

# Mapping Spiral Structure on the far side of the Milky Way

Alberto Sanna,<sup>1\*</sup> Mark J. Reid,<sup>2</sup> Thomas M. Dame,<sup>2</sup>  
Karl M. Menten,<sup>1</sup> Andreas Brunthaler<sup>1</sup>

<sup>1</sup>Max-Planck-Institut für Radioastronomie, Auf dem Hügel 69, 53121 Bonn, Germany,

<sup>2</sup>Harvard-Smithsonian Center for Astrophysics, 60 Garden Street, Cambridge, MA 02138, USA

\*E-mail: asanna@mpifr-bonn.mpg.de

**Little is known about the portion of the Milky Way lying beyond the Galactic center at distances of more than 9 kilo-parsec from the Sun. These regions are opaque at optical wavelengths due to absorption by interstellar dust, and distances are very large and hard to measure. We report a direct trigonometric parallax distance of  $20.4^{+2.8}_{-2.2}$  kilo-parsec obtained with the Very Long Baseline Array to a water maser source in a region of active star formation. These measurements allow us to shed light on Galactic spiral structure by locating the Scutum-Centaurus spiral arm as it passes through the far side of the Milky Way, and to validate a kinematic method for determining distances in this region based on transverse motions.**

Large scale maps of the Milky Way have had to exclude a triangular region with the Sun at its apex and extending  $\sim 10^\circ$  to either side of the Galactic center (e.g., (1)). In this region the Galaxy is rotating almost perpendicularly to our line-of-sight, so the radial velocities that enable the estimate of so-called kinematic distances are degenerate at values around zero. Some progress has been made in the nearer parts of this region with distances determined through stellar spectra and, more recently, parallax measurements for astronomical sources of maser emission from newly formed stars (2). But, the region behind the Galactic center has remained largely out of reach due to the large distances ( $> 9$  kpc), very high foreground extinction, and source confusion.

The Bar and Spiral Structure Legacy (BeSSeL) Survey is a Key Project of the Very Long Baseline Array (VLBA), which has been measuring trigonometric parallaxes and motions on the sky plane (hereafter, proper motions) of methanol and water masers associated with hundreds of high-mass star forming regions in the Galaxy. Recently, the project focused mainly on distant regions to locate distant segments of the Galactic spiral arms. Here, we discuss the most distant of these sources, G007.47+00.05 (or IRAS 17591–2228), for which an accurate parallax distance was not previously available. The source lies on the far side of the Galaxy and appears to link the prominent Scutum-Centaurus spiral arm in the fourth Galactic quadrant with a distant molecular arm recently discovered in the first quadrant, dubbed the Outer Scutum-Centaurus (OSC) arm (3).

We used the VLBA to observe strong H<sub>2</sub>O maser emission at 22.2 GHz from the star-forming region G007.47+00.05 between 2014 March and 2015 March (4). We modeled the relative position in time of compact maser spots, with respect to an extragalactic continuum source (Figure 1A), as the sum of the parallax signature (i.e., a sinusoid), caused by our changing vantage point as the Earth orbits the Sun, plus a linear motion of the star-forming region relative to the Sun in the E–W and N–S directions (Figure 1B). After removing the linear motion, the parallax effect inferred from this analysis (Figure 1C) yields a parallax angle of  $0.049 \pm 0.006$  milli-arcsecond (mas). This measurement corresponds to a distance of  $20.4^{+2.8}_{-2.2}$  kpc (66,500 ly) with an uncertainty of less than  $\pm 14\%$ . In Figure 2, we plot the Galactic position of G007.47+00.05, superposed on a plan view of the Milky Way, which shows the locations of prominent star-forming sites determined from trigonometric parallaxes.

We compare this result with an independent, statistical (Bayesian), distance estimate (5), derived by taking into account complementary information about the spatial distribution and kinematics of giant molecular clouds in the Galaxy. In Figure 3, we plot the probability density function (PDF) for the source distance, based on five distinct contributions (listed below), and the cumulative best estimate for the probability of any given distance (black solid line). The red solid line (PDF<sub>SA</sub>) quantifies the probability that a set of three values, Galactic longitude ( $\ell$ ), latitude ( $b$ ), and radial velocity with respect

to the local standard of rest (LSR),  $V_{\text{LSR}}$ , match those values expected for a given spiral arm segment, as traced by CO and HI emission (e.g. (6)). The loci of individual spiral arms are then fixed in position by trigonometric parallaxes, following previous analysis (2). Also plotted is the kinematic distance probability ( $\text{PDF}_{\text{KD}}$ ), as inferred from the radial velocity of the source with respect to the Sun ( $V_{\text{LSR}}$ ), after assuming a rotation curve for the Galaxy (2). Because star-forming regions are expected to lie close to the Galactic plane, we have also quantified the expectation of finding a source at high Galactic latitude if it is near the Sun, and vice versa ( $\text{PDF}_{\text{GL}}$ ). Details of how these contributions are calculated have been previously discussed (5).

In Figure 3, we assign two additional distance PDFs to the source, based on its proper motion in the Galactic latitude and longitude directions. The more distant the source, the smaller one expects the angular motion out of the plane ( $\text{PDF}_{\text{PM,b}}$ ). At the same time, the proper motion along the plane (i.e., in Galactic longitude) provides an additional kinematic distance probability ( $\text{PDF}_{\text{PM},\ell}$ ), which makes use of the velocity component ( $V_{\perp}$ ) perpendicular to the line-of-sight (e.g. (7)). The probability density function,  $\text{PDF}_{\text{PM},\ell}$ , is generated similarly to the  $\text{PDF}_{\text{KD}}$  (5, *their section 2.2*). The observed proper motion components ( $\mu_x, \mu_y$ ) are rotated about the line-of-sight into Galactic components ( $\mu_\ell, \mu_b$ ), and the component projected along the Galactic longitude ( $\mu_\ell$ ) is compared with that expected under the assumption of circular Galactic orbits as a function of distance (e.g. eq. 4 of (7)). This calculation of kinematic distance using proper motions is most effective toward the Galactic center and anticenter, the directions in which conventional kinematic distances based on radial velocities are least useful. A similar calculation was previously followed by (8), who estimated for G007.47+00.05 a far kinematic distance of  $20 \pm 2$  kpc (see supplementary online text). These authors made use of the Japanese VERA (VLBI Exploration of Radio Astrometry) array to observe the H<sub>2</sub>O maser emission between March 2009 and December 2011.

Evaluating the kinematic distance PDFs requires Bayesian priors for the Galactic rotation curve,  $\Theta(R)$ , and the fundamental Galactic parameters of the circular rotation speed  $\Theta_0$  at the distance  $R_0$  of

the Sun from the Galactic center. In Table 1, we list the priors and source input data used to calculate the PDFs. For the  $V_{\text{LSR}}$  of the source, we adopt the average velocity of the  $\text{H}_2\text{O}$  maser emission of  $-16 \pm 4 \text{ km s}^{-1}$ , which is consistent with the peak of radio recombination lines at  $-16.9 \pm 0.1 \text{ km s}^{-1}$  (9) and the range of CS emission at  $-13.9 \pm 4.6 \text{ km s}^{-1}$  (10). For the proper motion of the star-forming region  $(\mu_x, \mu_y)$ , we averaged the final values derived from Figure 1 ( $-2.42 \pm 0.02 \text{ mas yr}^{-1}$ ,  $-4.64 \pm 0.30 \text{ mas yr}^{-1}$ ) with those measured by (8) based on three masers ( $-2.46 \pm 0.14 \text{ mas yr}^{-1}$ ,  $-4.38 \pm 0.14 \text{ mas yr}^{-1}$ ). Since residual atmospheric delays between the target and calibration source usually dominate the uncertainty in proper motion measurements, and the three masers likely have the same systematic uncertainties, we have inflated by  $\sqrt{3}$  the proper motion uncertainties from (8), to account for fully correlated motions among the masers. This analysis provides a proper motion in Galactic longitude  $(\mu_\ell)$  of  $-5.12 \pm 0.18 \text{ mas yr}^{-1}$ .

In Figure 3, we show that the combined Bayesian distance of  $20.4 \pm 0.6 \text{ kpc}$  agrees well with our trigonometric parallax measurement. However, some caveats should be noted. Kinematic distances hold under the assumption of purely circular orbits. This condition is not satisfied within about 4 kpc of the Galactic center, where the gravitational effects of the Milky Way’s central bar cause highly non-circular motions (e.g. (11, 12)). A line of sight from the Sun at  $\ell = 7.47^\circ$  passes through this region between 4.7 and 12.3 kpc; hence this range of distances cannot be excluded based on kinematic PDFs. Our direct parallax measurement does not suffer this limitation.

The spiral arm PDF ( $\text{PDF}_{\text{SA}}$ ) has two main peaks between 4 and 5 kpc, because the target source has a  $V_{\text{LSR}}$  between that of the Norma ( $\sim 10 \text{ km s}^{-1}$ ) and Near 3-kpc ( $-20 \text{ km s}^{-1}$ ) arms at that longitude (e.g. Figure 7 of (12)); the current parallax measurement unambiguously rules out such small distances. Distances to spiral arms beyond about 10 kpc are a substantial extrapolation because of the current lack of direct parallax measurements. The spiral arm PDF shows a small peak at  $\sim 16 \text{ kpc}$  based on a long extrapolation of the Outer arm (red curve in Figure 2) through the first Galactic quadrant. However, locating G007.47+00.05 at this distance can be excluded by the parallax distance, with a probability of

> 95%, as well as by kinematic distance values, since this portion of the Outer arm is well outside the Galactic center region.

Close to the Galactic plane at a longitude of  $7.5^\circ$  (e.g. Figure 3 of (3)), the OSC arm has a  $V_{\text{LSR}}$  ( $-12 \text{ km s}^{-1}$ ) close to that of the target source. If the Scutum-Centaurus arm is a logarithmic spiral with constant pitch angle ( $\psi$ ) of  $14^\circ$ , which is constrained by the tangent directions of the Scutum ( $\ell = 31^\circ$ ) and Centaurus ( $\ell = 309^\circ$ ) arms in addition to nearby parallax measurements (3), the distance to the OSC arm at the longitude of the maser source would be in the range 20–21 kpc. In Figure 2, we show the logarithmic spiral of the OSC arm under these conditions. This arm also coincides, within the uncertainties, with the farthest arm traced by (13), taking into account the value of  $R_0$  adopted by those authors. This distance estimate determines a third peak of the  $\text{PDF}_{\text{SA}}$  which is consistent with the trigonometric parallax distance. In Figure 3, the combination of spiral and (both) kinematic PDFs strongly constrains a narrow range of distances (absolute peak of the black solid line), which matches the trigonometric distance of 20.4 kpc.

This result has two further consequences. First, the agreement of the parallax and the kinematic distances can be interpreted as evidence that the approximation of circular motions holds at Galactocentric radii near 12 kpc in the far outer Galaxy. Second, it calls into question the assumption of constant pitch angle of the Outer Scutum-Centaurus arm along its winding around the Galaxy. In Figure 2, we extend the track of the Scutum segment from the first Galactic quadrant through the fourth quadrant, by assuming a logarithmic spiral with  $\psi$  of  $20^\circ$ . This pitch angle provides the best spiral fit to trigonometric distances of star-forming regions in the Scutum arm between  $\ell$  of  $5.9^\circ$  and  $32.0^\circ$  (14, 15). Because the near segment of the Scutum-Centaurus arm (i.e., the Scutum arm in the first quadrant) has a much larger pitch angle than that determined from the Scutum and Centaurus tangents and the location of G007.47+00.05 ( $14^\circ$ ), it is clear that a single logarithmic spiral cannot describe the full complexity of the Scutum-Centaurus-OSC arm. This result is in agreement with a recent analysis of the spiral arm morphology in four external face-on galaxies, where pitch angles can vary along individual arms by more

than  $10^\circ$  (16).

In summary, we have measured the distance to a water maser source in the OSC arm using both a direct trigonometric parallax and a statistical Bayesian analysis. Our parallax distance agrees with an indirect distance estimate for the source inferred from its measured (proper) motion on the sky (8), thus providing support for the determination of kinematic distances based on proper motions rather than radial motions alone. These measurements allow us to trace the Scutum-Centaurus arm nearly one full turn of Galactic azimuth and out to large Galactocentric radii on the far side of the Milky Way, and shows that we can map spiral structure throughout the Galaxy.

## References and Notes

1. J. H. Oort, F. J. Kerr, G. Westerhout, *Mon. Not. R. Astron. Soc.* **118**, 379 (1958).
2. M. J. Reid, *et al.*, *Astrophys. J.* **783**, 130 (2014).
3. T. M. Dame, P. Thaddeus, *Astrophys. J.* **734**, L24 (2011).
4. Materials and methods are available as supplementary materials on Science Online.
5. M. J. Reid, T. M. Dame, K. M. Menten, A. Brunthaler, *Astrophys. J.* **823**, 77 (2016).
6. T. M. Dame, D. Hartmann, P. Thaddeus, *Astrophys. J.* **547**, 792 (2001).
7. Y. Sofue, *Publ. Astron. Soc. Jpn.* **63**, 813 (2011).
8. A. Yamauchi, *et al.*, *Publ. Astron. Soc. Jpn.* **68**, 60 (2016).
9. D. S. Balser, R. T. Rood, T. M. Bania, L. D. Anderson, *Astrophys. J.* **738**, 27 (2011).
10. L. Bronfman, L.-A. Nyman, J. May, *Astron. Astrophys. Suppl. Ser.* **115**, 81 (1996).
11. J. Binney, O. E. Gerhard, A. A. Stark, J. Bally, K. I. Uchida, *Mon. Not. R. Astron. Soc.* **252**, 210 (1991).
12. A. Sanna, *et al.*, *Astrophys. J.* **781**, 108 (2014).
13. H. Nakanishi, Y. Sofue, *Publ. Astron. Soc. Jpn.* **68**, 5 (2016).
14. M. Sato, *et al.*, *Astrophys. J.* **793**, 72 (2014).
15. V. Krishnan, *et al.*, *Astrophys. J.* **805**, 129 (2015).
16. Z. N. Honig, M. J. Reid, *Astrophys. J.* **800**, 53 (2015).
17. M. Elitzur, ed., *Astronomical masers*, vol. 170 of *Astrophysics and Space Science Library* (1992).

18. M. J. Reid, M. Honma, *Annu. Rev. Astron. Astrophys.* **52**, 339 (2014).
19. A. T. Deller, S. J. Tingay, M. Bailes, C. West, *Publ. Astron. Soc. Pac.* **119**, 318 (2007).
20. G. van Moorsel, A. Kembball, E. Greisen, *Astronomical Data Analysis Software and Systems V*, G. H. Jacoby, J. Barnes, eds. (1996), vol. 101 of *Astronomical Society of the Pacific Conference Series*, p. 37.
21. M. J. Reid, *et al.*, *Astrophys. J.* **693**, 397 (2009).
22. M. Kettenis, H. J. van Langevelde, C. Reynolds, B. Cotton, *Astronomical Data Analysis Software and Systems XV*, C. Gabriel, C. Arviset, D. Ponz, S. Enrique, eds. (2006), vol. 351 of *Astronomical Society of the Pacific Conference Series*, p. 497.
23. M. Honma, Y. Tamura, M. J. Reid, *Publ. Astron. Soc. Jpn.* **60**, 951 (2008).
24. Y. W. Wu, *et al.*, *Astron. Astrophys.* **566**, A17 (2014).
25. A. Sanna, *et al.*, *Astrophys. J.* **745**, 191 (2012).
26. M. A. Trinidad, *et al.*, *Mon. Not. R. Astron. Soc.* **430**, 1309 (2013).
27. R. A. Burns, T. Handa, T. Nagayama, K. Sunada, T. Omodaka, *Mon. Not. R. Astron. Soc.* **460**, 283 (2016).
28. Y. Sofue, *et al.*, *Astrophys. J.* **523**, 136 (1999).
29. A. L. Fey, *et al.*, *Astron. J.* **127**, 3587 (2004).
30. K. Immer, *et al.*, *Astrophys. J. Suppl. Ser.* **194**, 25 (2011).
31. A. Sanna, *et al.*, *Astron. Astrophys.* **517**, A71 (2010).

**Acknowledgements:** A.S. gratefully acknowledges financial support by the Deutsche Forschungsgemeinschaft (DFG) Priority Program 1573. The National Radio Astronomy Observatory is a facility of the National Science Foundation operated under cooperative agreement by Associated Universities, Inc. This work made use of the Swinburne University of Technology software correlator, developed as part of the Australian Major National Research Facilities Programme and operated under license. The authors thank M. Honma for fruitful discussions in preparation. **Data and materials availability:** All data used in the paper are public available through the National Radio Astronomy Observatory (NRAO) archive under program BR198, at <https://archive.nrao.edu/archive/advquery.jsp>. A spectrum of the maser emission on 2014 March 18 can be found at [http://bessel.vlbi-astrometry.org/first\\_epoch](http://bessel.vlbi-astrometry.org/first_epoch).

### **Supplementary Materials**

[www.sciencemag.org](http://www.sciencemag.org)

Materials and Methods

Supplementary Text

Figures 4, 5

Tables 2, 3, 4

References (17–31) [Note: The numbers refer to any additional references cited only within the Supplementary Materials]

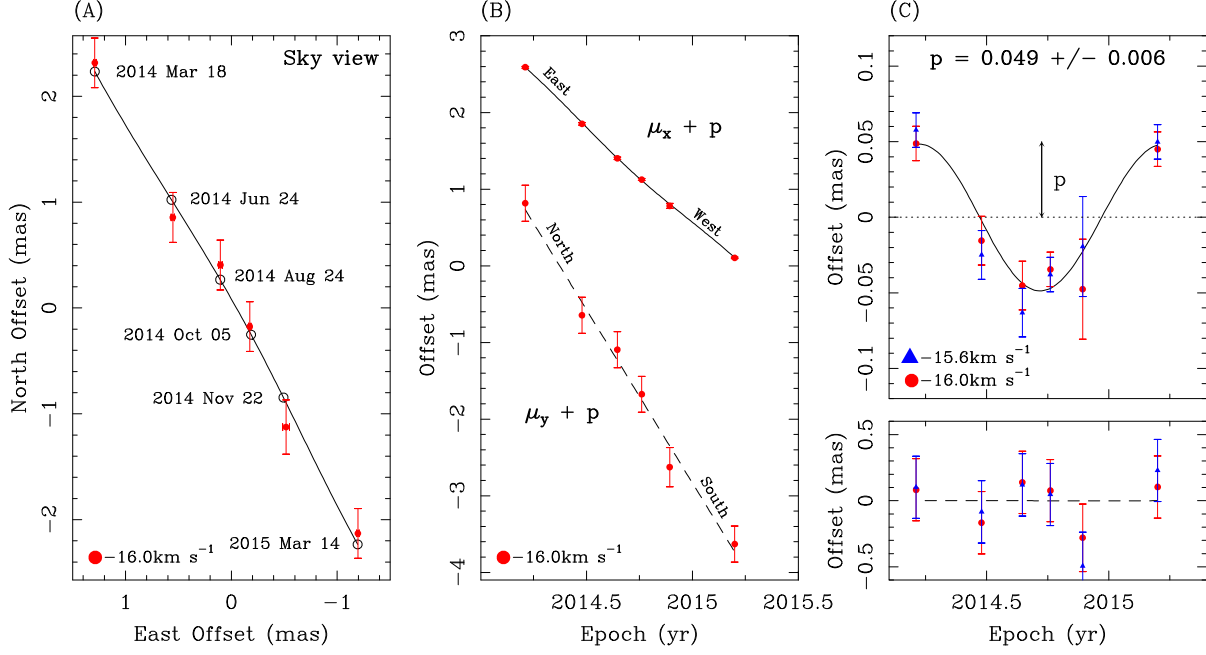


Figure 1: **Results of the combined parallax fit for G007.47+00.05.** This fit is obtained from the combination of two point-like maser spots with respect to the background quasar J175526.28–223210.6 (or [IBR2011]J1755–2232; Table S2). For clarity, we draw only maser positions for the spot at  $V_{\text{LSR}}$  of  $-16.0 \text{ km s}^{-1}$  (red circles). (A) Sky projected motion of the maser source with respect to J175526.28–223210.6 with each epoch labeled (the zero position is arbitrary). The empty circles and the line show the best-fitting position offsets and the trajectory, respectively. East offset uncertainties are smaller than the symbol. (B) Decomposed offset positions for the maser source along the east and north directions versus time. The best-fitting models in east and north directions are shown as continuous and dashed lines, respectively. (C) Same as the middle panel but with fitted proper motions subtracted ( $\mu_x$  and  $\mu_y$ ), yielding the parallax sinusoid. Positions for the spot at  $V_{\text{LSR}}$  of  $-15.6 \text{ km s}^{-1}$  are also shown for the final parallax ( $p$ ). The east offset (upper panel) and north offset (lower panel) data are shown separately on different scales.

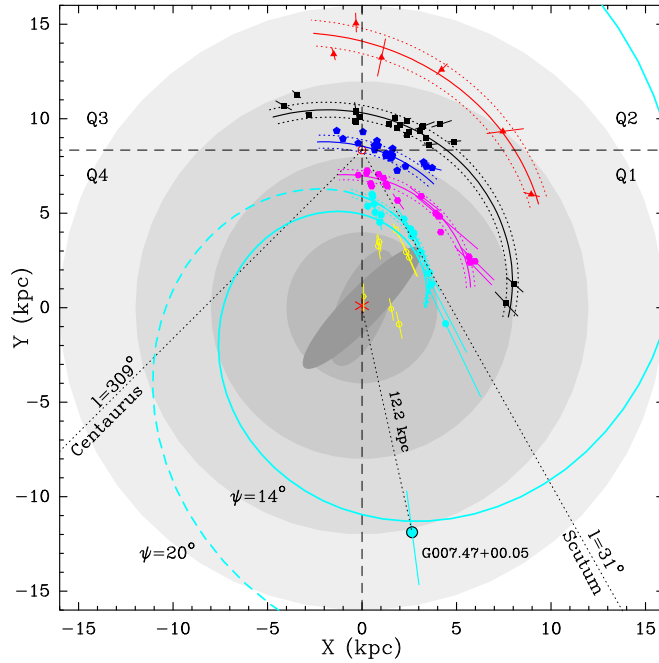


Figure 2: **Plan view of the Milky Way showing the location of G007.47+00.05 and other maser sources determined via trigonometric parallaxes (2, their Table 1).** The reference system gives offset positions from the Galactic center (red asterisk). Colored symbols designate distinct regions in the Galaxy: inner Galaxy sources (empty yellow circles); Scutum-Centaurus arm (solid cyan circles); Sagittarius arm (magenta hexagons); Local arm (blue pentagons); Perseus arm (black squares); Outer arm (red triangles). Error bars correspond to distance uncertainties of  $1\sigma$ . The background gray disks, centered on the Galactic center, show regions within Galactocentric radii of 4, 8, 12, and 16 kpc. The Sun is located at (0, 8.34) kpc. Galactic quadrants, centered on the Sun, are indicated with dashed lines. Solid lines trace log-periodic spiral fits to sources grouped by arms; dotted lines correspond to  $1\sigma$  widths. Two logarithmic spirals are drawn for the Scutum-Centaurus arm, one with a pitch angle ( $\psi$ ) of  $14^\circ$  (solid), constrained by the Scutum and Centaurus tangent directions (3), and the other with a pitch of  $20^\circ$  (dashed), based on maser sources in the inner first quadrant (14). The Scutum and Centaurus tangent directions are also shown. (Adapted from (2), their Figure 1).

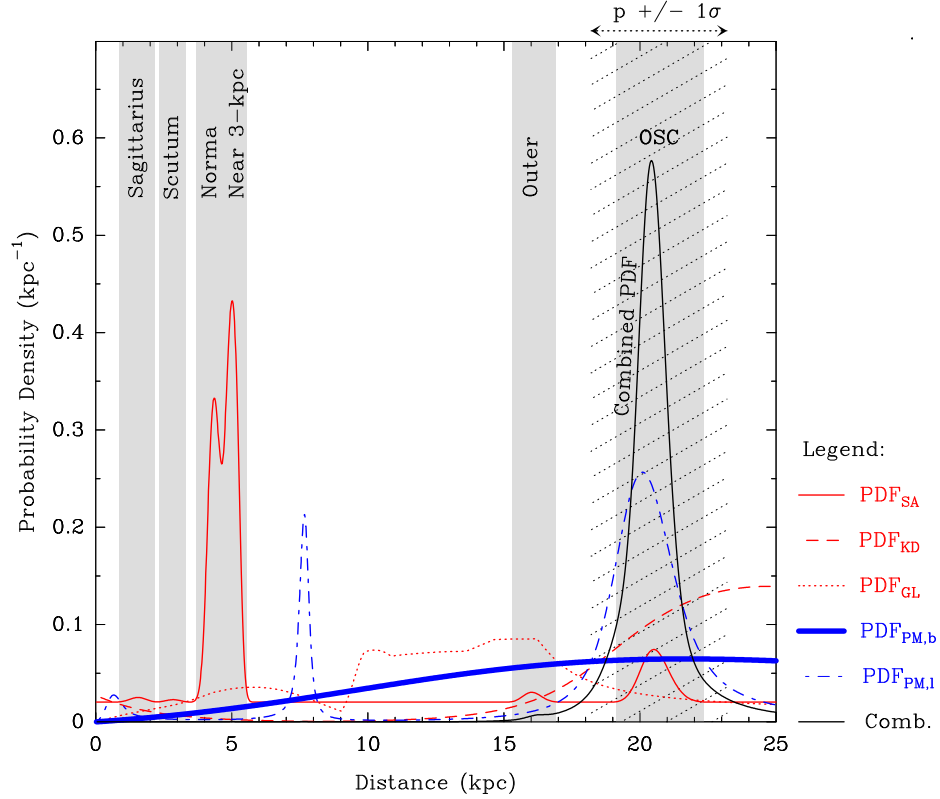


Figure 3: **Distance probability density function (PDF) for the star-forming region G007.47+00.05.** Individual PDFs are indicated by subscripts and refer to the spiral arm assignment of the source (SA), its kinematic distance (KD), Galactic latitude (GL), and its proper motion in latitude (PM,  $b$ ) and longitude (PM,  $\ell$ ). Input parameters for the PDFs are given in Table 1. Grey areas mark the expected regions for each spiral arm at a Galactic longitude of  $7.5^\circ$ . The combined PDF (black solid line) strongly favors an association with the Outer Scutum-Centaurus (OSC) arm at a distance of  $20.4 \pm 0.6$  kpc. This estimate agrees with the trigonometric parallax distance of  $20.4^{+2.8}_{-2.2}$  kpc (hatched black area).

Table 1: **Parameters used to calculate the distance PDFs.** Column 1 gives the type of Galactic rotation curve adopted for the calculation (2, *their Table 5*). Columns 2 and 3 report the fundamental Galactic parameters of circular rotation speed at the Solar circle and the distance of the Sun from the Galactic center, respectively (2). Columns 4 and 5 give the Galactic coordinates of the source in the longitude and latitude directions, respectively. Columns 6, 7, and 8 give the local standard of rest velocity of the source, and its motions on the sky plane, respectively.

$\Theta(R)$	Priors		Input Data				
	$\Theta_0$ ( $\text{km s}^{-1}$ )	$R_0$ (kpc)	$\ell$ ( $^\circ$ )	$b$ ( $^\circ$ )	$V_{\text{LSR}}$ ( $\text{km s}^{-1}$ )	$\mu_x$ ( $\text{mas yr}^{-1}$ )	$\mu_y$ ( $\text{mas yr}^{-1}$ )
Univ.	$241 \pm 8$	$8.34 \pm 0.16$	7.471	0.058	$-16 \pm 4$	$-2.44 \pm 0.07$	$-4.51 \pm 0.17$

## Supplementary Materials

### Materials and methods

#### Observations and Calibration

We conducted VLBA observations of the  $6_{16} - 5_{23}$   $\text{H}_2\text{O}$  maser emission line (e.g. (17); rest frequency 22.235080 GHz) towards the star-forming region G007.47+00.05. Six separate observations were performed over the course of one year; observing dates are indicated in Figure 1A. Relative astrometric accuracy is inversely proportional to the angular separations of sources on the sky, so we selected three background sources (Table S1) located  $< 4^\circ$  from the maser as calibration points. At each epoch we observed for 7 hours and calibrated the atmospheric propagation path-delays for each antenna. Details of the observational strategy can be found in (18). Table S1 summarizes the source information.

Four adjacent intermediate frequency bands, each 16 MHz wide, were recorded in dual circular polarization; each band was correlated to produce 32 spectral channels. The third band was centered at the LSR velocity of the strongest maser feature ( $-16.0 \text{ km s}^{-1}$ ). This band was additionally correlated with 2000 spectral channels, each 8.0 kHz wide, in order to sample the maser linewidths with a velocity resolution of  $0.11 \text{ km s}^{-1}$ . The data were processed with the VLBA DiFX software correlator (19) using an integration time of 1 s.

Data were calibrated and imaged with the NRAO Astronomical Image Processing System (AIPS; e.g. (20)) following the procedure described in (21) and using the ParselTongue scripting interface (22). For the final imaging, we removed any data for which an antenna in an interferometer baseline had an elevation less than  $15^\circ$  above the horizon. In Figure S1, we show the images of the background sources from the first epoch, phase-referenced to the maser channel at  $V_{\text{LSR}}$  of  $-15.6 \text{ km s}^{-1}$ .

### **Parallax fitting**

Maser spots for parallax fitting were selected according to the following criteria: (1) spots persisting over the 6 epochs that belong to isolated cloudlets, in order to avoid emission blended between different maser centers; (2) compact maser spots, unresolved by the VLBA beam or slightly resolved but with a stable, deconvolved, position angle; (3) bright maser spots with signal-to-noise ratios of more than a hundred.

As described in the main text, we fitted the observations with an astrometric model that accounts for both parallax and proper motion of the source. Results of the parallax and proper motion fitting for two point-like maser spots with respect to J175526.28–223210.6, the calibration source projected nearest the maser, are listed in Table S2. The formal fitting uncertainties were combined in quadrature with error floors to account for the effects of unmodeled atmospheric delays. These error floors were set to  $\pm 0.005 \text{ mas}$  and  $\pm 0.23 \text{ mas}$  in the E–W and N–S directions, respectively, so as to yield values of reduced  $\chi^2$  (per degree of freedom) near unity for each coordinate (e.g. (21) for details). On 2014 November 22 only four antennas out of nine could be used for imaging (because of instrumental issues), with a maximum baseline length of  $\approx 2000 \text{ km}$ , and the formal position uncertainties were 3 times greater than at the other epochs (Figure 1C). We simultaneously fitted the positions of the two spots listed in Table S2, solving for a single parallax, but allowing for different proper motions. The final parallax uncertainty was multiplied by  $\sqrt{2}$  to account for the possibility of residual atmospheric delays between the maser and the calibrator line-of-sights, which would be fully correlated for the two maser spots. The combined parallax fit yielded a parallax of  $0.049 \pm 0.006 \text{ mas}$  and is shown in Figure 1C.

Note that, especially for sources at low declination, N–S components of relative positions often have greater uncertainties than the E–W components, mainly because systematic errors from unmodeled atmospheric delays are more strongly correlated with N–S positions (e.g. (23)). This effect is also well established by previous observations (e.g. (14, 24)), and the observing epochs are selected to optimally sample the sinusoidal parallax signature in right ascension.

Since the parallax uncertainty, established by the magnitude of the post-fit residuals, is fairly small, we now evaluate whether this is of the expected magnitude. At a frequency of 22 GHz, the dominant error in relative position measurements is due to residual tropospheric delays, which predominantly scale with the zenith angle between sources. The calibrator J175526.28–223210.6 has a negligible N–S offset with respect to the target source ( $\theta_N \sim 0$ , or a position angle, P.A., of  $90^\circ$ ). As shown by (23), an E–W alignment between calibrator and target source minimizes astrometric errors for low declination sources. According to their analysis, observations at a declination of  $-30^\circ$ , with the four stations of the Japanese VERA array, would provide single-epoch position errors of  $\pm 0.042$  mas in the E–W direction, for an E–W separation of  $1^\circ$  and 1 cm rms vertical path-delay uncertainty. For a source declination of  $+15^\circ$ , astrometric errors would be reduced to  $\pm 0.025$  mas under the same conditions. At the Declination of about  $-22^\circ$  of our sources and a maser-calibrator separation of  $1.6^\circ$ , one would therefore expect relative position errors of  $\approx 0.060$  mas. However, the VLBA provides twice the maximum baseline length of VERA (2300 km), as well as double the number of antennas, which should reduce position uncertainties by a factor  $1/(2 \times \sqrt{2})$ . Therefore, for our observations, we expect an E–W parallax uncertainty of  $0.060 \text{ mas} \times (1/(2 \times \sqrt{2})) \times 0.5 \times (1/\sqrt{6-3})$ , where the 0.5 factor comes from the fact that we measure the full parallax sinusoid (i.e., double the parallax angle), and  $\sqrt{6-3}$  is the degrees of freedom in the model. This estimate of the parallax uncertainty ( $\pm 0.006$  mas) is in agreement with the measured value.

We discarded parallax fits for the second and third calibration sources, both of which are projected more than  $3^\circ$  away from the target maser ( $\theta_N > 2^\circ$ ), because of high residual uncertainties in the E–W offsets. If we repeat the above calculation of expected parallax uncertainty for the calibrator

J180740.68–250625.9, taking into account its offset and position angle with respect to the maser source, we obtain an E–W position error of  $\pm 0.24 \text{ mas} \times (1/(2 \times \sqrt{2}))$  for a single epoch of VLBA observations. The same calculation for the calibrator J175141.34–195047.5 yields an E–W error of the same order. These predicted single-epoch errors are smaller, by a factor of about 2.5, than the error floors obtained from the parallax fit of the two calibration sources ( $\geq 0.2 \text{ mas}$ ). A posteriori, this result suggests that the astrometric errors introduced by the atmosphere at the large offsets of those two calibrators may be non-linear with the distance from the target.

### **Maser source and internal proper motions**

In Figure S2, we show the distribution of individual maser emission centers (or cloudlets) detected towards G007.47+00.05. Maser properties are reported in Table S3. The maser emission clusters at two positions, labeled as the northwestern (NW) and southeastern (SE) groups, which have an average separation of about 60 mas (or 1224 au, at the distance of 20.4 kpc). Their spatial distribution resembles the bipolar shocks previously reported in other sources (25, 26, 27). We measured the internal maser proper motions by applying a simple model of expansion between the NW and SE clusters of maser emission. We calculated the centroid position of the two groups of masers from those cloudlets which persist over 1 yr, and determined their median position at each epoch. We then assumed this median position as the best guess for the star position (Figure S2) and measured the relative motion of the maser cloudlets with respect to the star. These relative proper motions are drawn in Figure S2. The proper motion along the east-west and north-south directions ( $V_x, V_y$ ) of the maser spots at a  $V_{\text{LSR}}$  of  $-15.6 \text{ km s}^{-1}$  and  $-16.0 \text{ km s}^{-1}$ , which were used for the parallax measurements, are  $(-3.5, 9.8) \text{ km s}^{-1}$  and  $(-13.5, -6.2) \text{ km s}^{-1}$ , respectively. The uncertainty on each velocity component is  $0.8 \text{ km s}^{-1}$ . The proper motion of the central star that excites the maser spots was derived by correcting the combined fit values for the peculiar motion of the maser spots with respect to the central star (Table S2).

## Supplementary text

In the following, we comment on the proper motion measurements presented in Table S2 with respect to the values reported by (8, *their Table 3*). These authors observed the H<sub>2</sub>O maser emission from the star-forming region G007.47+00.05 over 3 yr. They conducted astrometric observations with the Japanese VERA array and measured the relative position in time of the H<sub>2</sub>O maser source with respect to the background calibrator J175526.28–223210.6, the same calibrator we observed with the VLBA. Because the VERA observations covered a time baseline three time longer than that of the VLBA observations, this difference would provide a higher accuracy in the proper motion measurements by a factor  $\sqrt{3}$ , under the same conditions. In the N–S direction, the VERA and VLBA observations have comparable positional uncertainties (cf. Figure 1C and Figure 4 of (8)), which are dominated by unmodeled atmospheric delays. Therefore, the N–S component of the proper motion ( $\mu_y$ ) determined with the VERA observations is more accurate by a factor  $\sim \sqrt{3}$  than that determined with the VLBA observations. On the other hand, in the E–W direction, the VLBA observations are more accurate by a factor  $\sim 20$  than the VERA observations (cf. Figure 1C and Figure 4 of (8)). Taking into account the different time baseline of the observations, the accuracy of the VLBA and VERA proper motions eventually differs by an order of magnitude in the E–W direction.

In this work, we corrected the proper motions determined from the parallax fitting by the internal motions of the maser distribution (see above). In the analysis by (8), they detected three maser cloudlets with negligible relative motions, and made a weighted averaged of the proper motions determined from the three masers (*their Table 3*). Because of the different methods, we used an arithmetic average to combined the proper motion determined in Table S2 with those by (8).

The distance estimated from the proper motion measurements by (8) is in agreement with the trigonometric parallax distance determined in this work. The uncertainty estimated by (8) for the “far” kinematic distance is also similar to that derived from the trigonometric parallax. These authors explored the effects

on the kinematic distance of changing  $\Theta(R)$  and/or the Solar motion values, and showed that the uncertainty on the circular rotation speed at the Sun ( $\Theta_0$ ) dominates the uncertainty of the kinematic distance. For example, an uncertainty of  $\pm 14 \text{ km s}^{-1}$  on  $\Theta_0$  corresponds to a distance uncertainty of  $\pm 1.2 \text{ kpc}$ . The same analysis applies to the sensitivity of the kinematic  $\text{PDF}_{\text{PM},\ell}$  on the choice of the priors.

On the other hand, a “near” kinematic distance could not be excluded a priori by (8). In addition to the expectation of large non-circular velocities in the Galactic center region, which might be able to produce any combination of proper motion and radial velocity, a ray from the Sun towards a longitude of  $7.47^\circ$  comes within about 1 kpc of the Galactic center. In external galaxies similar to the Milky Way, rotation curves significantly drop inward at small Galactocentric radii (e.g. (28)). Therefore, the circular rotation speed in the Galactic center region is likely far less than the value assumed by (8).

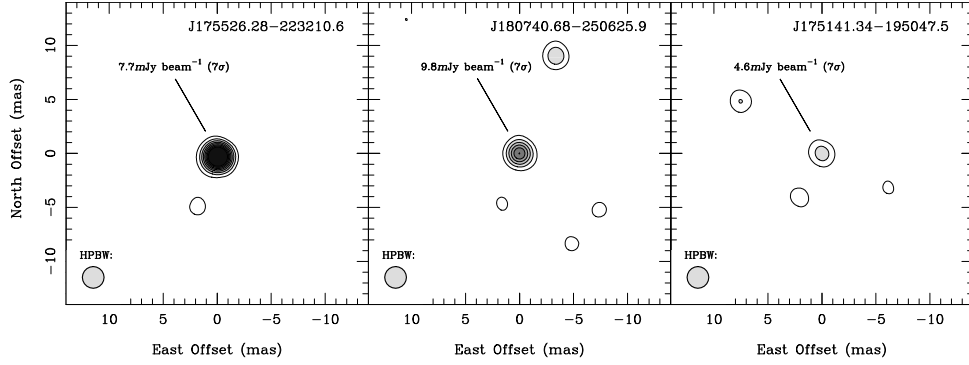


Figure 4: **Images of the calibration continuum sources at 22 GHz near the target maser.** The calibrators were phase-referenced to the maser channel at  $V_{\text{LSR}}$  of  $-15.6 \text{ km s}^{-1}$ . Offsets are given with respect to the brightness peak of each calibrator. Source names are indicated in the upper right corner and restoring beams are drawn in the lower left corner of each panel. Images are from the first epoch observations. Contour levels start at  $7\sigma$  in steps of  $7\sigma$  (see Table S1).

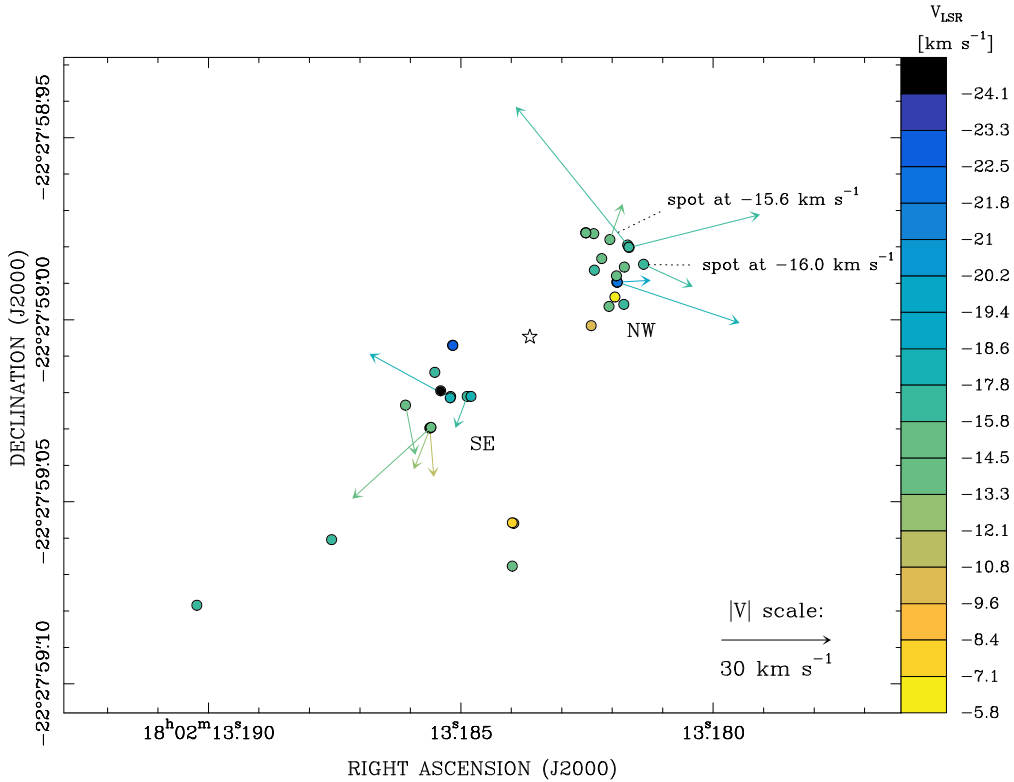


Figure 5: **Distribution (dots) and proper motions (arrows) of the  $\text{H}_2\text{O}$  maser cloudlets detected towards G007.47+00.05.** The color of each spot indicates the gas LSR velocity as given by the color bar. The proper motion scale is shown in the bottom right corner. The two main clusters of maser emission are labeled NW and SE. The white star between the NW and SE clusters marks the modeled position of the central exciting star. Positions of the two spots used for the parallax fitting are indicated.

Table 2: **Source Information.** Positions and source properties for the target maser and the background calibrators (29, 30), listed by increasing angular separation. The peak position of the phase-reference maser channel No. 997 on 2014 March 18 (first epoch) is given in columns 2 and 3 and is accurate to within  $\pm 1$  mas. We report the positions of the calibrators used at the VLBA correlator. Angular offsets in the east ( $\theta_E$ ) and north ( $\theta_N$ ) directions relative to the maser source are indicated in columns 4 and 5. Column 6 gives the restoring beam size (HPBW, round) used at each epoch. Columns 7 and 8 give the peak intensities ( $F_{\text{peak}}$ ) and the image rms noise of the phase-reference maser channel (at  $V_{\text{LSR}}$  of  $-15.6$ ) and 22 GHz background sources (from the first epoch data).

Sources (identifier)	R.A. (J2000) (h m s)	Dec. (J2000) ( $^{\circ}$ ' ")	$\theta_E$ ( $^{\circ}$ )	$\theta_N$ ( $^{\circ}$ )	HPBW (mas)	$F_{\text{peak}}$ (Jy beam $^{-1}$ )	Image rms (Jy beam $^{-1}$ )
G007.47+00.05 (IRAS 17591–2228)	18:02:13.1820	–22:27:58.978	...	...	2.0	12.67	0.047
J175526.28–223210.6 ([IBR2011]J1755–2232)	17:55:26.2848	–22:32:10.617	–1.57	–0.07	2.0	0.107	0.001
J180740.68–250625.9 ([IBR2011]J1807–2506)	18:07:40.6877	–25:06:25.943	1.26	–2.64	2.0	0.059	0.001
J175141.34–195047.5 ([IBR2011]J1751–1950)	17:51:41.3438	–19:50:47.506	–2.43	2.62	2.0	0.012	0.001

Table 3: **G007.47+00.05 – Parallax & Proper Motion modeled values.** Column 1 reports the LSR velocity of the reference maser spots at ch. 997 and 1001, respectively; column 2 indicates the calibration source whose data were used to model the relative proper motion of the masers; column 3 reports the fitted parallax; columns 4 and 5 give the fitted proper motions along the east and north directions, respectively. In the last row, we report the distance measurement inferred from the combined parallax fit. The Galactic proper motion of G007.47+00.05 was obtained by the combined fit value corrected for the internal proper motions of the maser source.

Maser $V_{\text{LSR}}$ (km s $^{-1}$ )	Calibration Source	Parallax (mas)	$\mu_x$ (mas yr $^{-1}$ )	$\mu_y$ (mas yr $^{-1}$ )
–15.6	J175526.28–223210.6	$0.052 \pm 0.007$	$-2.454 \pm 0.015$	$-4.540 \pm 0.303$
–16.0	J175526.28–223210.6	$0.044 \pm 0.005$	$-2.511 \pm 0.015$	$-4.516 \pm 0.303$
<b>Combined parallax &amp; corrected Galactic proper motion:</b>				
	$D = 20.4^{+2.8}_{-2.2}$ kpc	$0.049 \pm 0.006$	$-2.418 \pm 0.017$	$-4.639 \pm 0.303$

Table 4: **Parameters of the 22.2 GHz H<sub>2</sub>O maser cloudlets detected towards G007.47+00.05.** Each maser emission center is labeled by decreasing LSR velocity in Column 1. Columns 2 and 3 report the LSR velocity and peak brightness of each cloudlet at the first epoch of detection. Columns 4 and 5 give the relative centroid position of each cloudlet, and their uncertainties, in the east and north directions, respectively. The absolute position of the reference spot, belonging to cloudlet num. 16, is reported in Table S1. Details for the calculations of the maser cloudlet properties are given in (31). Columns 6 and 7 give the proper motion components of the cloudlets, with respect to the star, along the east and north directions, respectively. The relative position of the central star, with respect to cloudlet num. 16, is also indicated.

Feature #	$V_{\text{LSR}}$ (km s <sup>-1</sup> )	$F_{\text{peak}}$ (Jy beam <sup>-1</sup> )	$\Delta x$ (mas)	$\Delta y$ (mas)	$V_x$ (km s <sup>-1</sup> )	$V_y$ (km s <sup>-1</sup> )
1	-5.9	0.26	-1.39 ± 0.05	-15.76 ± 0.07	...	...
2	-7.6	0.22	26.79 ± 0.09	-77.76 ± 0.11	...	...
3	-10.0	0.53	26.40 ± 0.02	-77.90 ± 0.03	...	...
4	-10.7	0.24	5.13 ± 0.05	-23.63 ± 0.09	...	...
5	-11.4	1.41	49.46 ± 0.01	-51.75 ± 0.01	-1.1 ± 1.4	-13.4 ± 1.5
6	-12.7	0.94	49.34 ± 0.01	-51.70 ± 0.01	4.5 ± 1.9	-11.4 ± 2.0
7	-13.4	0.25	-1.81 ± 0.07	-9.95 ± 0.09	...	...
8	-13.5	0.50	56.13 ± 0.03	-45.47 ± 0.04	-2.7 ± 4.3	-13.7 ± 5.3
9	-13.7	0.50	49.11 ± 0.02	-51.57 ± 0.02	21.6 ± 10.6	-19.6 ± 13.3
10	-14.1	0.31	0.23 ± 0.05	-18.35 ± 0.07	...	...
11	-14.9	0.27	6.60 ± 0.10	1.85 ± 0.12	...	...
12	-15.1	0.51	6.61 ± 0.03	1.91 ± 0.03	...	...
13	-15.1	0.33	2.24 ± 0.08	-5.21 ± 0.10	...	...
14	-15.3	0.29	-3.97 ± 0.08	-7.55 ± 0.13	...	...
15	-15.4	0.37	26.80 ± 0.07	-89.68 ± 0.12	...	...
16	-15.6	12.85	0.00 ± 0.01	0.01 ± 0.01	-3.5 ± 0.7	9.8 ± 0.8
17	-15.7	0.82	4.42 ± 0.03	1.65 ± 0.04	...	...
18	-15.9	2.56	-4.88 ± 0.02	-1.49 ± 0.02	30.7 ± 1.6	38.0 ± 1.8
19	-16.0	6.08	-9.26 ± 0.01	-6.77 ± 0.01	-13.5 ± 0.8	-6.2 ± 0.9
20	-16.0	0.42	-3.84 ± 0.06	-17.79 ± 0.10	...	...
21	-16.1	0.39	76.43 ± 0.09	-82.41 ± 0.12	...	...
22	-16.4	1.32	39.19 ± 0.02	-43.06 ± 0.02	3.2 ± 2.1	-8.7 ± 2.2
23	-16.4	0.57	113.44 ± 0.02	-100.42 ± 0.02	...	...
24	-16.6	0.40	-5.17 ± 0.04	-2.05 ± 0.06	...	...
25	-16.8	0.37	4.26 ± 0.03	-8.39 ± 0.04	...	...
26	-17.1	0.74	-5.29 ± 0.02	-2.14 ± 0.03	-36.0 ± 7.9	9.0 ± 10.2
27	-17.2	0.29	48.09 ± 0.04	-36.45 ± 0.07	...	...
28	-17.2	0.20	43.74 ± 0.14	-43.09 ± 0.15	...	...
29	-18.2	0.74	43.85 ± 0.02	-43.45 ± 0.02	22.2 ± 2.8	12.1 ± 3.1
30	-18.2	0.56	38.14 ± 0.03	-43.07 ± 0.03	...	...
31	-18.4	1.93	-1.92 ± 0.01	-11.63 ± 0.01	-33.7 ± 1.1	-11.3 ± 1.2
32	-19.3	1.02	-1.97 ± 0.01	-11.70 ± 0.01	-9.2 ± 1.8	0.5 ± 1.9
33	-21.9	0.37	-2.05 ± 0.03	-11.68 ± 0.05	...	...
34	-22.6	0.27	43.12 ± 0.05	-29.06 ± 0.08	...	...
35	-22.5	0.53	43.20 ± 0.03	-29.02 ± 0.03	...	...
36	-24.9	0.57	46.48 ± 0.02	-41.52 ± 0.02	...	...
Star			21.99 ± 0.01	-26.70 ± 0.01		